Electrical circuit modeling and analysis of microwave acoustic interaction with biological tissues

Gao, Fei; Zheng, Qian; Zheng, Yuanjin

2014

https://hdl.handle.net/10356/105278

https://doi.org/10.1118/1.4871783

Electrical Circuit Modeling and Analysis of Microwave Acoustic Interaction with Biological Tissues

Fei Gao, Yuanjin Zheng, and Qian Zheng

School of Electrical and Electronic Engineering, Nanyang Technological University, 639798, Singapore

5

Purpose: Numerical study of microwave imaging and microwave-induced thermoacoustic imaging utilizes finite difference time domain (FDTD) analysis for simulation of microwave and acoustic interaction with biological tissues, which is time-consuming due to complex grid-segmentation and numerous calculations, not straightforward due to no analytical

10   solution and physical explanation, and incompatible with hardware development requiring circuit simulator such as SPICE.. In this paper, instead of conventional FDTD numerical simulation, an equivalent electrical circuit model is proposed to model the microwave acoustic interaction with biological tissues for fast simulation and quantitative analysis in both one and two dimensions (2D).

15   **Methods:** The equivalent circuit of ideal point-like tissue for microwave-acoustic interaction is proposed including transmission line, voltage-controlled current source, envelop detector, and resistor-inductor-capacitor (RLC) network, to model the microwave scattering, thermal expansion and acoustic generation. Based on which, 2-port network of the point-like tissue is built and characterized using pseudo S-parameters and transducer gain. Two dimensional

20   circuit network including acoustic scatterer and acoustic channel is also constructed to model the 2D spatial information and acoustic scattering effect in heterogeneous medium.

Results: Both FDTD simulation, circuit simulation, and experimental measurement are performed to compare the results in terms of time domain, frequency domain, and pseudo S-parameters characterization. 2D circuit network simulation is also performed under different

25   scenarios including different sizes of tumors and the effect of acoustic scatterer.

Conclusions: The proposed circuit model of microwave acoustic interaction with biological tissue could give good agreement with FDTD simulated and experimental measured results. The pseudo S-parameters and characteristic gain could globally evaluate the performance of tumor detection. The 2D circuit network enables the potential to combine the quasi-numerical

30   simulation and circuit simulation in a uniform simulator for co-design and simulation of a

microwave acoustic imaging system, bridging bio-effect study and hardware development seamlessly.

I. INTRODUCTION

Early detection of tumor before its spreading to other healthy tissues is extremely important to the survival rate of cancer patients[1]. As an emerging non-invasive imaging modality, microwave acoustic imaging, including microwave imaging (MI) and microwave-induced thermoacoustic imaging (TAI), is attracting more and more attention especially for breast cancer detection. Based on the significant dielectric contrast between tumor and healthy tissues[2-4], non-invasive microwave acoustic imaging is expected to provide high contrast performance with lower cost and more safety than existing imaging modalities such as MRI and X-ray CT. High specificity of microwave acoustic imaging modality is also desired to differentiate malignant and benign tumors, which have much low dielectric contrast[5]. Multi-modality imaging combining MI and TAI is expected to achieve higher performance than any one of them[6-8].
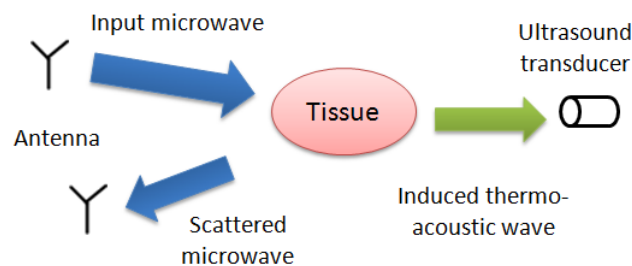

Fig. 1. Microwave acoustic interaction with biological tissues, including microwave scattering, EM energy absorption followed by the thermoacoustic effect and acoustic wave generation.

For both microwave imaging (such as microwave tomography and confocal microwave imaging) and microwave-induced thermoacoustic imaging, microwave signal is transmitted into biological tissues and interacting with the tumor. The scattered microwave signal is received by the antenna placed around the biological tissues for microwave imaging[9-14], and the acoustic signal induced by microwave absorption and thermal expansion is detected by ultrasound transducers for thermoacoustic imaging[15-21], as shown in Fig. 1. Finite difference time domain (FDTD) analysis is widely used to solve the Maxwell's equation for simulating EM and acoustic propagation and interaction in the biological tissues when studying these microwave acoustic imaging modalities[22], providing accurate wideband and time-domain simulation for beamforming and image reconstruction. However, FDTD simulation is time-consuming when simulating long time duration, and separated simulation is needed for EM

2

and acoustic field in microwave-induced thermoacoustic imaging research[23-24]. In addition, as a numerical simulation method, it is not capable of evaluating the imaging system performance quantitatively. To our best knowledge, there is no uniform model and simulation approach integrating the numerical simulation for microwave acoustic bio-effect with circuit simulation for microwave acoustic imaging hardware development.

In previous literature, to predict the thermoacoustic resonance effect with experimental validation, Gao *et al.*[21] proposed to use a simple series resistor-inductor-capacitor (RLC) electrical circuit to model the resonance response with preliminary simulation results. In this paper, an complete equivalent circuit model with more rigorous derivation and significant circuit model extension, comprehensive FDTD/circuit simulation and experimental results is proposed primarily for microwave-acoustic interaction and simulation with biological tissues in point-like and two dimensional circuit network, bridging bio-effect study and hardware development seamlessly. Based on rigorous derivation and reasonable simplification, parameters in the biological domain involving microwave scattering, absorption, thermoelastic expansion and acoustic generation, are well mapped into circuit parameters. Fast simulation using circuit simulators such as SPICE and ADS etc. is enabled and good agreement with the numerical simulation is achieved. Furthermore, considering the tumor circuit model as a 2-port network represented by pseudo S-parameters, source and load are added to involve antenna and ultrasound transducer matching problem. Transducer gain is introduced as the characteristic gain to comprehensively evaluate the performance of the microwave acoustic imaging modality. Co-design between hardware for microwave acoustic imaging system implementation and numerical simulation equivalently represented by the proposed circuit model is becoming possible and providing global optimization for a microwave acoustic imaging system design.

This paper is organized as follows. In section II, the equivalent circuit modeling for the microwave acoustic interaction is proposed with biological tissues. In section III, we extract the pseudo S-parameters of the tumor tissue's 2-port network and calculate the transducer gain considering source and load as the characteristic gain for microwave acoustic imaging system evaluation. In section IV, circuit and FDTD simulation results are in good agreement to show the validity of the proposed circuit model, together with experiment verification in section V. In section VI&VII, a 2D circuit network is proposed to include acoustic scattering effect in a heterogeneous medium, enabling circuit modeling and simulation of complex biological tissues, followed by the discussion and conclusion in section VIII.

3

II. CIRCUIT MODELLING OF MICROWAVE ACOUSTIC INTERACTION WITH BIOLOGICAL TISSUES

95   For microwave acoustic imaging modality, a microwave signal is transmitted into biological tissues from outside and undergoes the following four biophysical interactions: microwave reflection due to the dielectric contrast between tumor and healthy tissues; EM energy absorption and heating due to higher conductivity of the tumor tissue; tumor vibration and acoustic generation due to the thermo-elastic effect; and acoustic reflection due to the

100   acoustic impedance mismatch. The overall equivalent circuit model is shown in Fig. 2 and described in detail in the following parts.
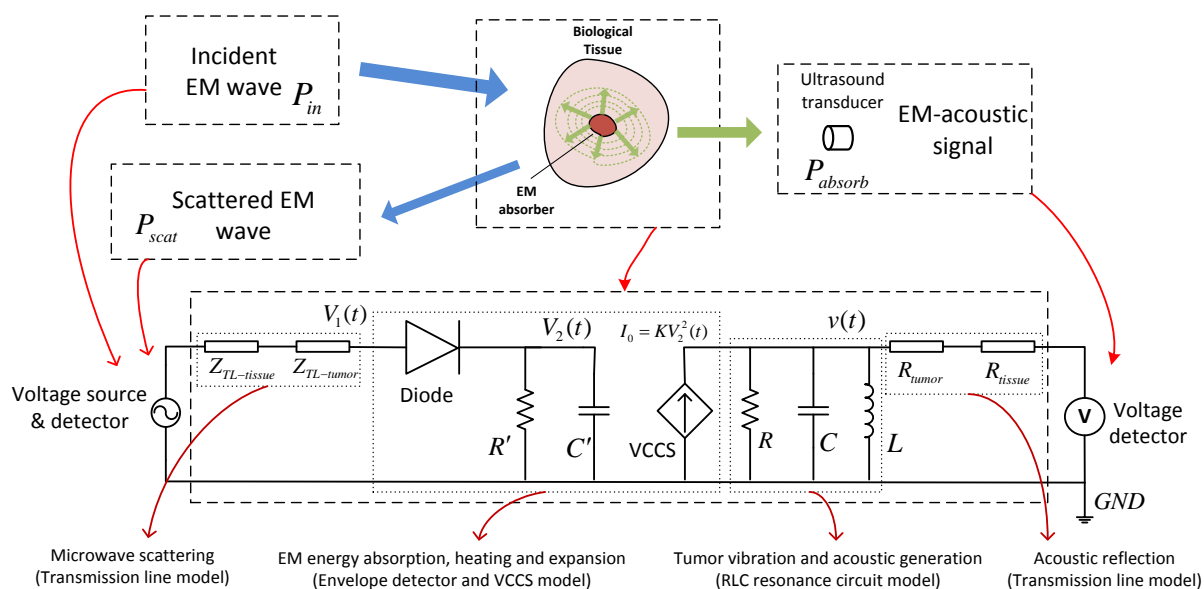
Fig. 2. The overall equivalent circuit modeling of microwave acoustic interaction with the biological tissues. Four biophysical interactions are separated by the dotted lines and modeled as transmission

105   line mismatch, envelope detector, voltage-controlled current source (VCCS), and parallel RLC resonance circuit. Tumor and surrounding healthy tissues are noted at the bottom.

II.A. Microwave scattering

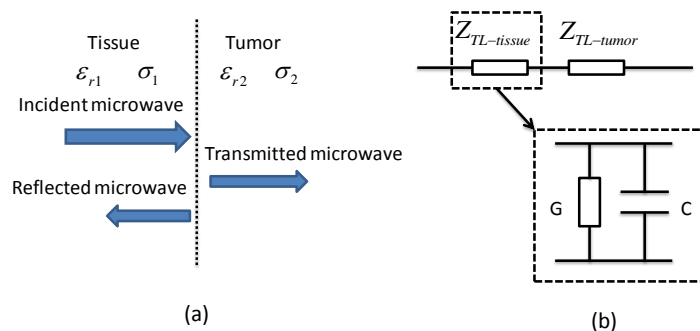(a)   (b)

4

Fig. 3. (a) Planar model for tumor and healthy tissue with different dielectric constant and (b) its equivalent circuit model represented by transmission line.

In order to simplify the complicated numerical simulation for microwave scattering in the biological tissues, we utilize the planar tissue model to demonstrate the reflection and transmission phenomenon at the interface of two mediums with different intrinsic impedance Z_{tissue} shown in Fig. 3(a)[25]:

$$Z_{tissue} = \sqrt{\frac{\mu}{\varepsilon}} = \sqrt{\frac{\mu}{\varepsilon_r - j\dfrac{\sigma}{\omega\varepsilon_0}}} \qquad (1)$$

where μ is the permeability, ε is the complex permittivity of tissue, expressed by the permittivity of free space ε_0, the relative permittivity of tissue ε_r, the conductivity σ, and the angular frequency ω. The reflection and transmission coefficients are derived by[25]:

$$R_{microwave} = \left| \frac{Z_{tumor} - Z_{tissue}}{Z_{tumor} + Z_{tissue}} \right| \qquad (2)$$

$$T_{microwave} = \left| \frac{2Z_{tumor}}{Z_{tumor} + Z_{tissue}} \right|. \qquad (3)$$

Similarly, microwave propagation in transmission line also follows above equations, where the tissue's intrinsic impedance Z_{tissue} is equivalent to the characteristic impedance of transmission line $Z_{TL\text{-}tissue}$ in Fig. 3(b). So we propose:

$$Z_{TL-tissue} = Z_{tissue}. \qquad (4)$$

By modeling the transmission line as a lumped capacitance and conductance in parallel, the characteristic impedance of transmission line is further expressed as:

$$Z_{TL-tissue} = \frac{1}{G + j\omega C}. \qquad (5)$$

Substitute Eq. (1) and (5) into Eq. (4):

$$\frac{1}{G + j\omega C} = \sqrt{\frac{\mu}{\varepsilon_r - j\dfrac{\sigma}{\omega\varepsilon_0}}} \qquad (6)$$

then, we have:

$$\mu(G + j\omega C)^2 = \varepsilon_r - j\frac{\sigma}{\omega\varepsilon_0}. \qquad (7)$$

To obtain the relationship between tissue dielectric parameters (permittivity, conductivity) and transmission line parameters (conductance, capacitance), we equalize the real and imaginary parts of Eq. (7) respectively:

$$\mu\left(G^2 - \omega^2 C^2\right) = \varepsilon_r \qquad (8)$$

$$j\mu 2G\omega C = -j\frac{\sigma}{\omega\varepsilon_0} \qquad (9)$$

then we have:

$$\mu\omega^2 C^2 = \mu G^2 - \varepsilon_r \qquad (10)$$

$$\mu 2G\omega^2 C = -\frac{\sigma}{\varepsilon_0}. \qquad (11)$$

By solving equations (10) and (11), we obtain the expressions of lumped capacitance and conductance of the transmission line in terms of tissues' permittivity and conductivity:

$$C^2 = \frac{-\varepsilon_r + \sqrt{\varepsilon_r^2 + \dfrac{\sigma^2}{\omega^2\varepsilon_0^2}}}{2\mu\omega^2} \qquad (12)$$

$$G^2 = \frac{\varepsilon_r + \sqrt{\varepsilon_r^2 + \dfrac{\sigma^2}{\omega^2\varepsilon_0^2}}}{2\mu}. \qquad (13)$$

Now the transmission line model of biological tissues for microwave scattering is established and linked with dielectric parameters determined by tissues' permittivity and conductivity using Eq. (12) and (13).

II.B. EM energy absorption, tissue heating and expansion

Apart from microwave scattering at the interface of tumor and healthy tissues, EM energy absorption also exists inside the tumor, where conductivity is larger than the surrounding tissues due to higher water content. Following the tissue heating and thermal expansion, initial acoustic pressure $p_0(\vec{r}, t)$ is induced by a pulsed microwave illumination, expressed as[17]:

$$p_0(\vec{r},t) = \Gamma(\vec{r})A(\vec{r})I(t) \tag{14}$$

where $\Gamma(\vec{r}) = \beta c^2 / C_P$ is the Gruneisen coefficient at position $\vec{r}$, β is the isobaric volume expansion coefficient, C_P is the specific heat and c is the acoustic velocity propagating in the tissue. $A(\vec{r})$ is the EM energy absorbed by a unit volume tissue at the position $\vec{r}$, and $I(t)$ is the envelope of the microwave pulse. $H(\vec{r},t) = A(\vec{r})I(t)$ is the heating function, the heating source of initial acoustic pressure. Then we introduce the specific absorption rate (SAR) expressed as: $SAR(\vec{r},t) = \sigma(\vec{r})|E(\vec{r},t)|^2 / 2\rho(\vec{r})$, where $\sigma(\vec{r})$ is the conductivity, $\rho(\vec{r})$ is the tissue density, and $|E(\vec{r},t)|$ is the temporal envelope of electric field at the position $\vec{r}$. Heating function can also be expressed as $H(\vec{r},t) = \rho(\vec{r})SAR(\vec{r},t)$ [26], then we have:

$$p_0(\vec{r},t) = \Gamma(\vec{r})H(\vec{r},t) = \Gamma(\vec{r})\frac{\sigma(\vec{r})}{2}|E(\vec{r},t)|^2. \tag{15}$$

In order to model the above process of converting temporal microwave energy to mechanical energy (initial pressure), an envelope detector circuit is proposed to extract the temporal envelope of the electrical field $E(\vec{r},t)$, followed by a voltage-controlled current source (VCCS), which converts the EM energy $|E(\vec{r},t)|^2$ to the initial acoustic pressure $p_0(\vec{r},t)$ linking the parameters in Eq. (15).

Shown in Fig. 2, a typical envelope detector circuit structure is chosen with a diode, capacitor and resistor. The value of capacitor and resistor is carefully selected to make sure that the output $V_2(t)$ of the envelope detector accurately follows the envelope of input signal:

$$V_2(t) = |E(\vec{r},t)|. \tag{16}$$

To represent the energy transformation from the EM wave to the initial acoustic wave, a voltage-controlled current source (VCCS) is introduced converting from voltage to current with a conversion ratio K. By this way, the electric field intensity and initial pressure are expressed by the voltage $V_2(t) = |E(\vec{r},t)|$ and the current $I_0(t) = p_0(\vec{r},t)$ respectively. According to Eq. (15) and (16), the VCCS is formulated by:

$$I_0(t) = p_0(\vec{r},t) = KV_2(t)^2 \tag{17}$$

7

$$K = \frac{1}{2}\Gamma(\vec{r})\sigma(\vec{r}). \qquad (18)$$

Up to now, the initial acoustic pressure has been modeled as $I_0(t)$ that is pumped by a voltage-controlled current source (VCCS).

II.C. Tumor vibration and acoustic generation

Starting from the radiative transport equation and Navier-Stokes equation, a general wave equation is obtained for the photoacoustic pressure in a tissue medium[27-28]:

$$\frac{1}{c^2}\frac{\partial^2}{\partial t^2}p(\vec{r},t) = \nabla^2 p(\vec{r},t) + \frac{\xi + \frac{4}{3}\eta}{\rho(\vec{r})c^2}\frac{\partial}{\partial t}\nabla^2 p(\vec{r},t)$$

$$-\frac{\xi + \frac{4}{3}\eta}{\rho(\vec{r})c^2}\Gamma(\vec{r})\nabla^2 H(\vec{r},t) + \frac{\Gamma(\vec{r})}{c^2}\frac{\partial H(\vec{r},t)}{\partial t} \quad (19)$$

where η is the shear viscosity, ξ is the bulk viscosity, c is the acoustic velocity, $\rho(\vec{r})$ is the tissue density, and $H(\vec{r},t)$ is the heat function. For thermoacoustic effect that we are interested here, the heating source is a pulsed microwave with heat function expressed as:

$$H(\vec{r},t) = \frac{\sigma(\vec{r})}{2}|E(\vec{r},t)|^2. \qquad (20)$$

Firstly we consider homogeneous small-size tumor model as a point source with the constant $\sigma(\vec{r})$ and $|E(\vec{r},t)|$ along spatial dimension (extension analysis to imaging will be discussed later), we have:

$$\nabla^2 H(\vec{r},t) = 0. \qquad (21)$$

Then substituting Eq. (15) and (21) into Eq. (19) achieves:

$$\frac{\partial^2}{\partial t^2}p(\vec{r},t) = c^2\nabla^2 p(\vec{r},t) + \frac{\xi + \frac{4}{3}\eta}{\rho(\vec{r})}\frac{\partial}{\partial t}\nabla^2 p(\vec{r},t) + \frac{\partial p_0(\vec{r},t)}{\partial t}. \qquad (22)$$

Assume that the acoustic pressure at position $\vec{r}$ could be expressed as $p(\vec{r},t) = e^{iar}p(t)$ [28], where a is the wave number, then Eq. (22) is simplified to:

$$\frac{\partial^2}{\partial t^2} p(t) + \frac{\xi + \frac{4}{3}\eta}{\rho(\vec{r})} \frac{\partial}{\partial t} p(t) + c^2 p(t) = \frac{1}{a^2} \frac{\partial p_0(\vec{r},t)}{\partial t}. \quad (23)$$

175   To accurately model the above second order differential pressure equation, a parallel RLC structure shown in Fig. 2 is brought in the circuit model. Interestingly, in this parallel RLC circuit pumped by the current source modeled as VCCS mentioned above, the source current and output voltage also follow the similar second order differential equation shown below:

$$\frac{\partial^2}{\partial t^2} v(t) + \frac{1}{RC} \frac{\partial}{\partial t} v(t) + \frac{1}{LC} v(t) = \frac{1}{C} \frac{\partial I_0(t)}{\partial t}. \quad (24)$$

It is worth noting that Eq. (23) and Eq. (24) have fundamentally physical relationship in
180   terms of the damped harmonic oscillation, which is a widely existing physical phenomenon in nature. More specifically, Eq. (23) and Eq. (24) can be treated as mechanical and electrical damped harmonic oscillations, respectively. Comparing Eq. (23) and Eq. (24), it is intuitive to equalize $v(t) = p(t)$ and $I_0(t) = p_0(\vec{r},t)$, then we map the parameters in these two equations one by one:

$$\begin{aligned} \frac{1}{a^2} &= \frac{1}{C} \\ \frac{\xi + \frac{4}{3}\eta}{\rho(\vec{r})} &= \frac{1}{RC} \\ c^2 &= \frac{1}{LC}. \end{aligned} \quad (25)$$

185   Solving Eq. (25), we have:

$$\begin{aligned} C &= a^2 \\ L &= \frac{1}{c^2} \\ R &= \frac{\rho(\vec{r})}{(\xi + \frac{4}{3}\eta)}. \end{aligned} \quad (26)$$

According to Eq. (26), the value of each circuit element is obtained from biological parameters in terms of acoustic velocity, tissue density, propagation phase constant and viscosity. In order to analytically solve the second order differential equation (24), The current source term $\partial I_0(t)/\partial t$ of the parallel RLC circuit is expressed as $Q_0\delta(t)$, where $\delta(t)$
190   is impulse function, then the explicit solution is derived as[29]:

$$v(t) = \frac{Q_0}{C} \frac{\omega_0}{\omega_d} \exp(-\alpha t) \cos\left(\omega_d t + \tan^{-1}\left(\frac{\alpha}{\omega_d}\right)\right) \quad (27)$$

where $Q_0 = |I_0|$ is the amplitude of the impulse source, and

$$\omega_0 = \sqrt{\frac{1}{LC}} = c \quad (28)$$

$$\alpha = \frac{1}{2RC} = \frac{\xi + \frac{4}{3}\eta}{2\rho(\vec{r})} \quad (29)$$

$$\omega_d = \sqrt{\omega_0^2 - \alpha^2} = \sqrt{c^2 - \left(\frac{\xi + \frac{4}{3}\eta}{2\rho(\vec{r})}\right)^2}. \quad (30)$$

Then substitute Eq. (28)-(30) into Eq. (27), we obtain the amplitude of Eq. (27) expressed by $|v(t)|$ in terms of biological parameters:

$$|v(t)| = |I_0| \frac{1}{\sqrt{1 - \left(\frac{\xi + \frac{4}{3}\eta}{2c\rho(\vec{r})}\right)^2}} \exp\left(-\frac{\xi + \frac{4}{3}\eta}{2\rho(\vec{r})} t\right). \quad (31)$$

Now the microwave-induced thermoacoustic signal $p(t)$ is modeled as $v(t)$ shown in Fig. 2 by Eq. (27)-(31).

II.D. Acoustic reflection

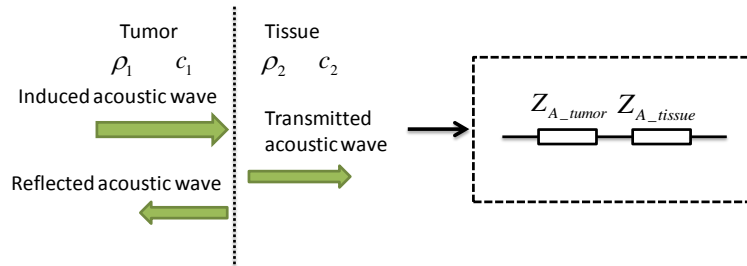Fig. 4. Planar model for tumor and healthy tissues with different acoustic impedance represented by transmission line in circuit modeling.

Similar with microwave propagation in biological tissues, the acoustic signal reflection also exists at the interface of two biological tissues (tumor and healthy tissue) with different acoustic impedance R_{tumor} and R_{tissue} shown in Fig. 4. Equivalent to Eq. (2)-(4), the reflection and transmission coefficient for acoustic impedance mismatch are[30]:

$$R_{acoustic} = \left| \frac{R_{tumor} - R_{tissue}}{R_{tumor} + R_{tissue}} \right|$$

$$T_{acoustic} = \left| \frac{2R_{tumor}}{R_{tumor} + R_{tissue}} \right| \quad\quad (32)$$

$$R_{tumor} = \rho_1 c_1, R_{tissue} = \rho_2 c_2.$$

Transmission line with same characteristic impedance as tissue's acoustic impedance is used to model the acoustic mismatch.

III. CHARACTERISTIC GAIN FOR MICROWAVE ACOUSTIC IMAGING

In this section, we extract the tumor circuit model that is established in the previous section to be a two-port network, to be represented by pseudo S-parameters. Incorporating source and load model together, a transducer gain is derived and proposed as a characteristic gain to evaluate the whole microwave acoustic imaging system.
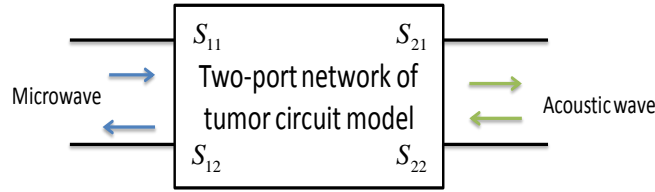

Fig. 5. Extracted two-port network of tumor circuit model represented by pseudo S-parameters.

III.A. Pseudo S-parameter extraction

In order to analyze the equivalent circuit model in top level, a two-port network is proposed to represent the tumor circuit model using pseudo S-parameters correlating microwave and acoustic parameters, which has similar formulation but totally different definition compared with scattering parameter in microwave community. As shown in Fig. 5, a microwave signal is reflected at the input port determined by S_{11} due to the dielectric contrast. The induced thermoacoustic wave is generated and reflected at the output port with the transmission coefficient S_{21} and the acoustic reflection coefficient S_{22} due to the acoustic impedance contrast. Because the thermoacoustic effect induced by pulse microwave illumination is irreversible, i.e. microwave cannot be generated by input acoustic pressure, the reverse transmission coefficient S_{12} is zero. In this case, this two-port network of the tumor model is unilateral. Recalling Eq. (2) for microwave reflection, we have:

11

$$S_{11} = \left| \frac{\dfrac{Z_{tumor}}{Z_{tissue}} - 1}{\dfrac{Z_{tumor}}{Z_{tissue}} + 1} \right|. \tag{33}$$

Substitute Eq. (1) into Eq. (33) using dielectric constant of tumor and healthy tissue ($\varepsilon_1, \varepsilon_2$), we obtain:

$$S_{11} = \left| \frac{\sqrt{\dfrac{\varepsilon_1}{\varepsilon_2}} - 1}{\sqrt{\dfrac{\varepsilon_1}{\varepsilon_2}} + 1} \right|. \tag{34}$$

It is clearly shown that S_{11} is determined by the difference of dielectric constant. Similarly, the acoustic reflection coefficient at the output port could be expressed as:

230

$$S_{22} = \left| \frac{\dfrac{R_{tumor}}{R_{tissue}} - 1}{\dfrac{R_{tumor}}{R_{tissue}} + 1} \right| \left| \frac{\dfrac{\rho_1 c_1}{\rho_2 c_2} - 1}{\dfrac{\rho_1 c_1}{\rho_2 c_2} + 1} \right| \tag{35}$$

and S_{22} is related with the acoustic impedance mismatch. To derive the transmission

235   coefficient S_{21}, we firstly substitute Eq. (17) and (18) into Eq. (31):

$$|v(t)| = \frac{1}{2} \Gamma(\vec{r}) \sigma(\vec{r}) V_2(t)^2 \frac{1}{\sqrt{1 - \left(\dfrac{\xi + \dfrac{4}{3}\eta}{2c\rho(\vec{r})} \right)^2}} \exp\left(-\frac{\xi + \dfrac{4}{3}\eta}{2\rho(\vec{r})} t \right). \tag{36}$$

We can calculate S_{21} as the transmission coefficient from the input microwave energy to the induced acoustic pressure due to the conductivity mismatch between the tumor and healthy tissues, then we have:

$$S_{21} = \frac{|v(t)|}{V_2(t)^2} = \frac{1}{2} \Gamma(\vec{r}) |\sigma_2(\vec{r}) - \sigma_1(\vec{r})| \frac{1}{\sqrt{1 - \left(\dfrac{\xi + \dfrac{4}{3}\eta}{2c\rho(\vec{r})} \right)^2}} \exp\left(-\frac{\xi + \dfrac{4}{3}\eta}{2\rho(\vec{r})} t \right). \tag{37}$$

From Eq. (37), we can easily find that S_{21} is mainly determined by two factors: conductivity

240    $\sigma(\vec{r})$ and viscosity $\xi + 4\eta/3$ of the tumor tissue, which refers to the microwave absorption

rate and attenuation term in (37), respectively. Finally the pseudo S-parameters of the proposed two-port network of tumor tissue are summarized in Eq. (38).

$$
\begin{pmatrix} S_{11} & S_{21} \\ S_{12} & S_{22} \end{pmatrix} = \begin{pmatrix} \left| \dfrac{\sqrt{\dfrac{\varepsilon_1}{\varepsilon_2}} - 1}{\sqrt{\dfrac{\varepsilon_1}{\varepsilon_2}} + 1} \right| & \dfrac{1}{2}\Gamma(\vec{r})\left|\sigma_2(\vec{r})-\sigma_1(\vec{r})\right| \dfrac{1}{\sqrt{1-(\dfrac{\xi+\dfrac{4}{3}\eta}{2c\rho(\vec{r})})^2}} \exp(-\dfrac{\xi+\dfrac{4}{3}\eta}{2\rho(\vec{r})}t) \\ \\ 0 & \left| \dfrac{\dfrac{\rho_1 c_1}{\rho_2 c_2} - 1}{\dfrac{\rho_1 c_1}{\rho_2 c_2} + 1} \right| \end{pmatrix} \qquad (38)
$$

III.B. Complete circuit model
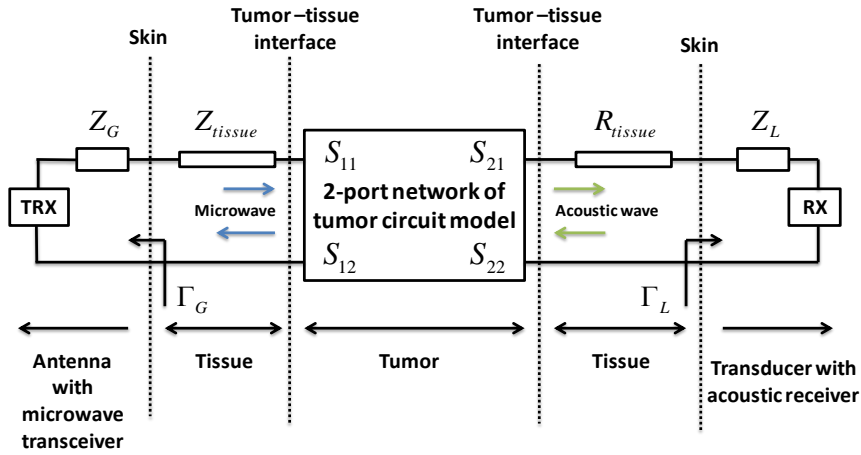
Fig. 6. Complete circuit model combining 2-port network of tumor represented by pseudo S-parameters, surrounding healthy tissue impedance Z_{tissue}, antenna and ultrasound transducer impedance Z_G, Z_L for EM and acoustic wave, together with microwave transceiver TRX and acoustic receiver RX. Reflection coefficient Γ_G and Γ_L represent impedance mismatch for microwave and acoustic wave at antenna and transducer sides respectively.

Added to the 2-port network of tumor circuit model represented by pseudo S-parameters, a more complete circuit model incorporating the impedance mismatch at the generator and load sides is proposed and shown in Fig. 6. In this complete circuit model, the surrounding healthy tissue along with skin tissue is modeled as transmission line with characteristic impedance Z_{tissue}. At the input side, source impedance Z_G is brought in to model the impedance of the antenna, which is assumed to be attached directly on the skin, and connected to microwave transceiver module (TRX) that is capable of transmitting input microwave and receiving

scattered microwave signal. Γ_G is the reflection coefficient at the input side representing the impedance mismatch between the antenna and the skin tissue, and expressed as:

$$\Gamma_G = \left| \frac{Z_G - Z_{tissue}}{Z_G + Z_{tissue}} \right|. \qquad (39)$$

At the load side, Z_L is used to model the acoustic impedance of ultrasound transducers, and Γ_L is describing the acoustic mismatch between the skin tissue and ultrasound transducers:

$$\Gamma_L = \left| \frac{Z_L - R_{tissue}}{Z_L + R_{tissue}} \right|. \qquad (40)$$

Acoustic receiver (RX) follows the ultrasound transducers for signal amplification and processing.

III.C. Transducer gain as characteristic gain

To analyze the complete circuit model, the transducer gain G_T [31] is engaged to be an indicator for tissue characterization and imaging, covering all the parameters in the model:

$$G_T = \frac{\left(1 - |\Gamma_G|^2\right)|S_{21}|^2\left(1 - |\Gamma_L|^2\right)}{\left|\left(1 - S_{11}\Gamma_G\right)\left(1 - S_{22}\Gamma_L\right) - S_{12}S_{21}\Gamma_G\Gamma_L\right|^2} \qquad (41)$$

substitute $S_{12} = 0$ into Eq. (41), we have:

$$G_T = \frac{\left(1 - |\Gamma_G|^2\right)|S_{21}|^2\left(1 - |\Gamma_L|^2\right)}{\left|\left(1 - S_{11}\Gamma_G\right)\left(1 - S_{22}\Gamma_L\right)\right|^2}. \qquad (42)$$

The transducer gain G_T incorporates S_{11}, S_{22}, S_{21}, Γ_G and Γ_L to fully characterize the complete 2-port network. Equivalently, the microwave scattering (S_{11}), the acoustic reflection (S_{22}), the thermoacoustic effect (S_{21}), the antenna skin mismatch (Γ_G) and the transducer-skin mismatch (Γ_L) are all incorporated into the transducer gain, which is defined as the characteristic gain to quantitatively characterize the microwave acoustic imaging modality.

Up to now, all the analysis above is based on the assumption that the tumor tissue is homogeneous and small enough to be modeled as a point. In order to extend the equivalent circuit model for real microwave acoustic imaging application, the biological tissue could be

14

partitioned into a number of small grids, within each grid the biological tissue is still eligible to be considered as a point model. By applying the proposed equivalent circuit model to fit each small grid of the biological tissue, similar with FDTD method assigning dielectric constant to each grid cell, it is potential to simulate the whole tissue imaging, which will be discussed in section VI. Furthermore, functional imaging is also possible by calculating the characteristic gain at each grid cell, which could fully characterize the microwave and acoustic properties of the tissue sample.
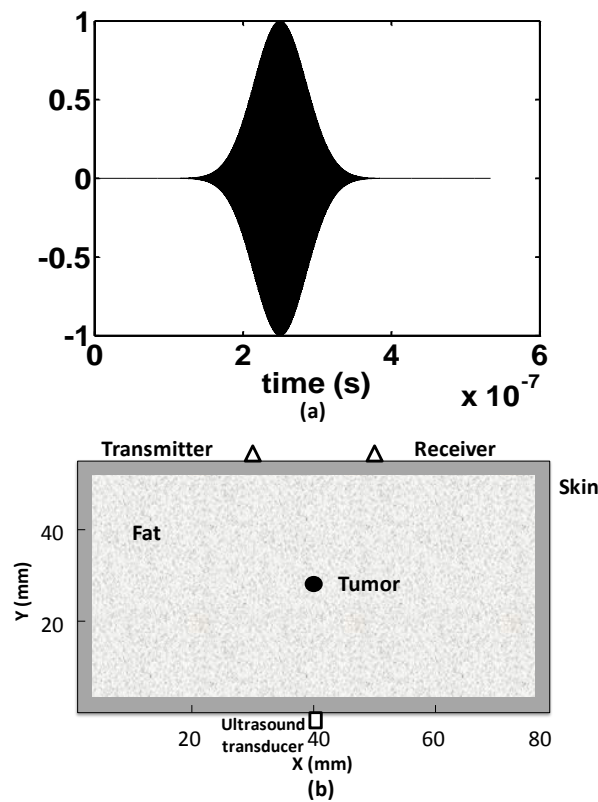
IV. SIMULATION

Fig. 7. (a) Gaussian modulated microwave source and (b) 2D numerical biological tissue model for EM and acoustic simulation.

In order to verify the validity of the equivalent circuit model established in the previous section, both numerical simulation and SPICE circuit simulation are conducted and compared. A Gaussian modulated microwave with 1 GHz central frequency and 0.1 μs pulse width is used to illuminate the biological tissues, shown in Fig. 7(a). The 2D numerical biological tissue structure for FDTD EM and acoustic simulation is demonstrated in Fig. 7(b), the homogeneous fat tissue is surrounded by the skin, and the tumor with 0.1mm diameter (as a

15

point source) is embedded in the center of the field. The microwave transmitter and receiver are placed at the top side and the ultrasound transducer is placed at the other side. The grid size of the FDTD simulation is 0.4 mm for the EM simulation and 0.1 mm for the acoustic simulation due to the much smaller wavelength of acoustic wave. Perfectly matched layer (PML) is utilized to terminate the computational region. In EM simulation, the scattered microwave is recorded by the receiver and the tumor response is calculated by subtracting the calibration signal recorded without the tumor. SAR is calculated at every grid cell and interpolated for the following acoustic simulation. Dielectric properties of tumor, skin and fat at 1GHz, are listed in table I, together with other biological parameters for FDTD numerical simulation[32]. Acoustic attenuation coefficient α is related with shear and bulk viscosity by[30]:

$$\alpha = \frac{2f^2\pi^2}{3\rho c^3}\left(\frac{4}{3}\eta + \xi\right). \tag{43}$$

Circuit element parameters are calculated based on the established equivalent circuit model and listed in table II. Some of the circuit parameters are only for tumor modeling and not applicable to other tissues, noted as N.A.. R' and C' are selected to extract the envelope of the microwave input properly. C is normalized as unity in the equivalent modeling.

TABLE I
PHYSICAL PARAMETERS OF BIOLOGICAL TISSUES

Tissue	Fat	Skin	Tumor
ε_0 (F/m)	8.85×10^{-12}	8.85×10^{-12}	8.85×10^{-12}
ε_r	5.4079	40.936	54.811
μ_0 (H/m)	$4\pi\times10^{-7}$	$4\pi\times10^{-7}$	$4\pi\times10^{-7}$
σ (S/m)	0.0528	0.8818	0.9782
ρ (kg/m^3)	1020	1100	1041
c (m/s)	1510	1537	1580
β (1/^oC)	3×10^{-4}	3×10^{-4}	3×10^{-4}
C_P (J/($^oC\cdot kg$))	3550	3550	3510
α (dB/cm)	0.75	3.5	0.57

TABLE II

EQUIVALENT CIRCUIT PARAMETERS OF THREE BIOLOGICAL TISSUES

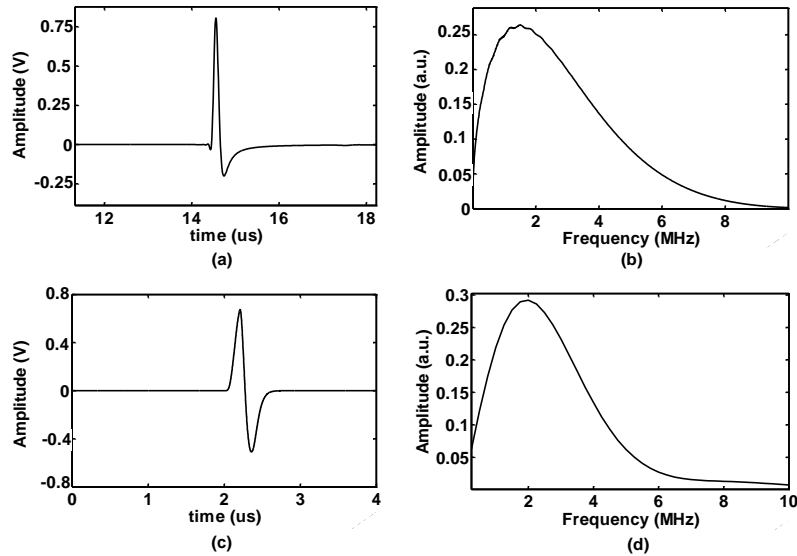| Tissue	Fat	Skin	Tumor
$Z_{TL-tissue}$ (Ohm)	$4.7660\times10^{-4}+$ $j4.1524\times10^{-5}$	$1.6631\times10^{-4}+$ $j3.1087\times10^{-5}$	$1.4597\times10^{-4}+$ $j2.2851\times10^{-5}$
$G_{TL-tissue}$ (S)	2082.4	5809.9	6686.8
$C_{TL-tissue}$ (F)	2.8875×10^{-8}	1.7284×10^{-7}	1.6660×10^{-7}
R_3 (Ohm)	N.A.	N.A.	1000
C_3 (F)	N.A.	N.A.	10×10^{-12}
K	N.A.	N.A.	3.5804×10^{5}
R (Ohm)	N.A.	N.A.	1.1706×10^{10}
L (H)	N.A.	N.A.	4.0058×10^{-7}
C (F)	N.A.	N.A.	1×10^{-6}
R_{tissue} (Ohm)	1.5402×10^{6}	1.6907×10^{6}	1.6448×10^{6}

310

Fig. 8. Numerical simulation (a)-(b) and circuit simulation (c)-(d) results of thermoacoustic signals in both time and frequency domain.

315   Numerical and circuit simulations are conducted separately using the FDTD and SPICE analysis. Time-domain simulation results are shown in Fig. 8(a), (c), where the acoustic waveforms generated from SPICE and FDTD simulation are in good agreement as N-shape pulse with comparable magnitude. The spectra of acoustic signals are shown in Fig. 8(b), (d)

with a similar central frequency and bandwidth. The validity of the equivalent circuit modeling is verified, and the minor difference between them is due to the simplicity of circuit modeling, e.g., the waveform of acoustic signals also depends on the actual size of the tumor, which is not taken into account in the equivalent circuit modeling here, but will be addressed in section VI in a 2D geometry.

TABLE III
SUMMARY OF TEN SIMULATION CASES WITH DIFFERENT DIELECTRIC CONTRAST

Dielectric constant of tumor at 1GHz ε_r =54.811, σ =0.9782 S/m			
Case	Normal tissue permittivity	Normal tissue conductivity (S/m)	Dielectric contrast
1	49.828	0.8893	1.1
2	45.676	0.8152	1.2
3	42.162	0.7525	1.3
4	39.151	0.6987	1.4
5	36.541	0.6521	1.5
6	34.257	0.6114	1.6
7	32.242	0.5754	1.7
8	30.451	0.5434	1.8
9	28.848	0.5148	1.9
10	27.406	0.4891	2.0

In another set of comparable simulations, the dielectric contrast between the tumor tissue and surrounding normal tissues is set to be variable, and summarized in table III. S_{11} and S_{21} are obtained, as well as the transducer gain G_T, which is defined as the characteristic gain for microwave acoustic imaging system. Shown in Fig. 9, when the dielectric contrast is increasing for both the numerical and circuit simulation, S_{11} and S_{21} are increasing together with the transducer gain (characteristic gain). The changing trends of the pseudo S-parameter and characteristic gain with dielectric contrast variation are coincident in both simulations, which is compatible with physical principles of microwave acoustic imaging as well.
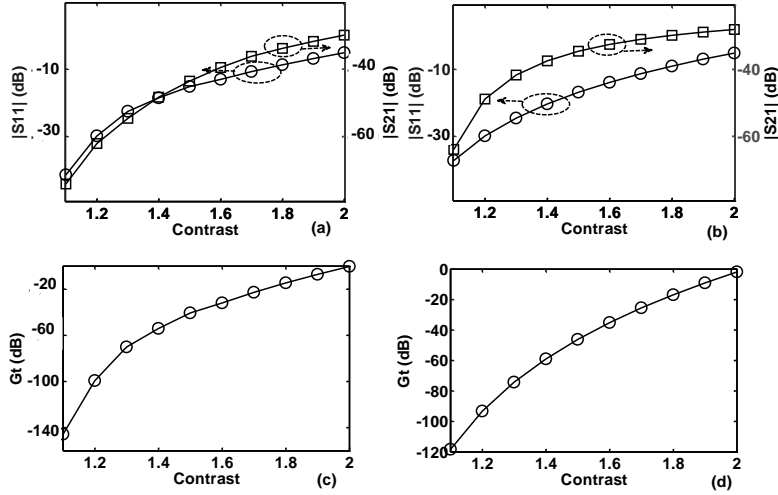
Fig. 9. Magnitude of S_{11} and S_{21} of numerical simulation (a) and circuit simulation (b) and their respective characteristic gain in (c)-(d) as a function of dielectric contrasts.

It is obvious that collecting both S_{11} and S_{21} is appreciated to maximize the characteristic gain. From Fig. 9 (a)-(b), we see that for the contrast ranging from 1.2 to 1.8, about 20 dB (numerical simulation) and 22 dB (circuit simulation) increase are obtained. However, the characteristic gain achieves about 80 dB and 75 dB respectively, which implies a significant sensitivity enhancement with the characteristic gain than S11 or S21 only. It predicts that the combination of microwave imaging and microwave-induced thermoacoustic imaging is expected to offer enhanced performance, which has been researched by numerical simulations in very recent work for benign and malignant tumor differentiation[6-7]. Interestingly, according to the expression (42) of the transducer gain, it is intuitive to see that S_{11}, S_{21}, and S_{22} are preferred to be large, together with preferred small Γ_G and Γ_L. Combining of photoacoustic or thermoacoustic with ultrasound imaging has also been proposed recently, which is to maximize S_{21} and S_{22} at the same time[33-35]. To maximize the characteristic gain, a new medical imaging modality, which combines microwave imaging, thermoacoustic imaging and ultrasound imaging together, is supposed to improve the performance further. On the other hand, minimizing Γ_G and Γ_L refers to the minimum reflection at the skin for microwave and acoustic propagation. Antennas attached to the skin is expected to specifically designed for the microwave acoustic imaging modality with high power coupling efficiency, such as in[36]. Meanwhile, ultrasound transducers should also be designed with similar acoustic impedance of the skin to reduce the acoustic reflection at the skin surface[37].
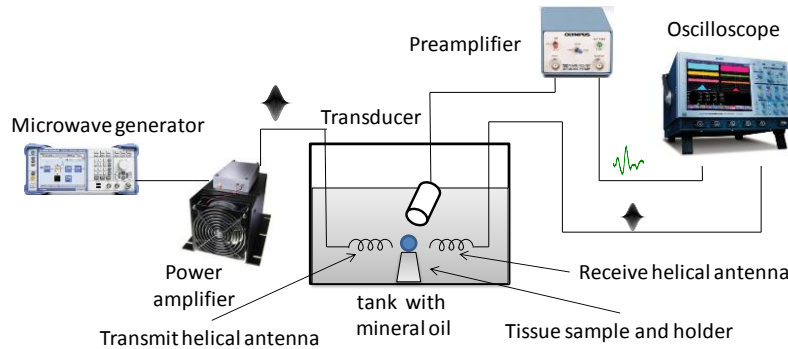
V. EXPERIMENTAL VERIFICATION

Fig. 10. Experimental setup capable of collecting both scattering microwave and induced thermoacoustic wave simultaneously.
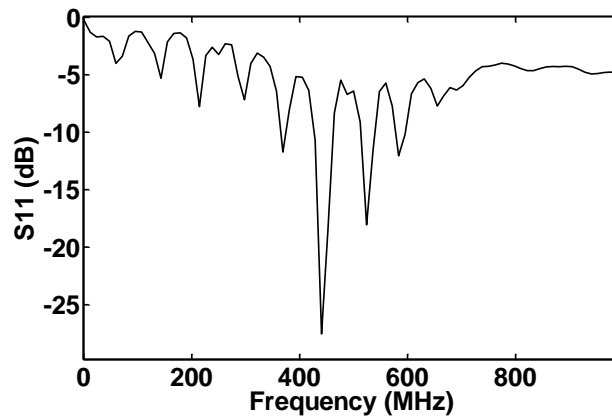
Fig. 11. Measured S_{11} of the custom-designed antenna.

In order to further verify the validity of the proposed equivalent circuit modeling, we build an experimental setup, which is capable of collecting scattering microwave signals and induced thermoacoustic signals simultaneously. Shown in Fig. 10, a microwave generator (SMBV100A, Rohde & Schwarz) under the amplitude shift keying (ASK) configuration is used to provide Gaussian pulse modulated microwave, which is amplified up to 100 W peak power by a microwave power amplifier (ZHL-100W-GAN+, Mini-Circuits). Due to the power and bandwidth limit (up to 100W and 500 MHz) of the power amplifier, we choose 440 MHz as carrier frequency and 2 μs pulse width so as to deliver up to 0.2 mJ/pulse into biological tissues, achieving 200 J/m^3 energy density within the 1 cm^2 antenna aperture and 1 cm radiation range. The pulse repetition rate is 10 Hz, leading to an average microwave power of 2 mW, which is much below the safety limit. The amplified Gaussian modulated microwave is fed into a custom-designed helical antenna with narrow radiation pattern at the

20

output and operating at 440 MHz, whose measured S11 is plotted in Fig. 11. Meanwhile, the
375   scattered microwave signal is received by another helical antenna placed at the other side, and the thermoacoustic signal due to the microwave absorption is also collected by an ultrasound transducer (V323-SU, Olympus) with 2.25 MHz central frequency, followed by an ultrasound preamplifier with 54 dB gain (Model 5662, Olympus). Both the scattered microwave and thermoacoustic signals are recorded with a digital oscilloscope (WaveMaster
380   8000A, Lecroy) at 5 G samples/s rate. In the tank, both the microwave antennas and the ultrasound transducer are immersed in mineral oil ($\varepsilon_r = 2.1, \sigma \approx 0$). The tissue sample is placed near the end of the transmitting helical antenna for maximum microwave illumination.
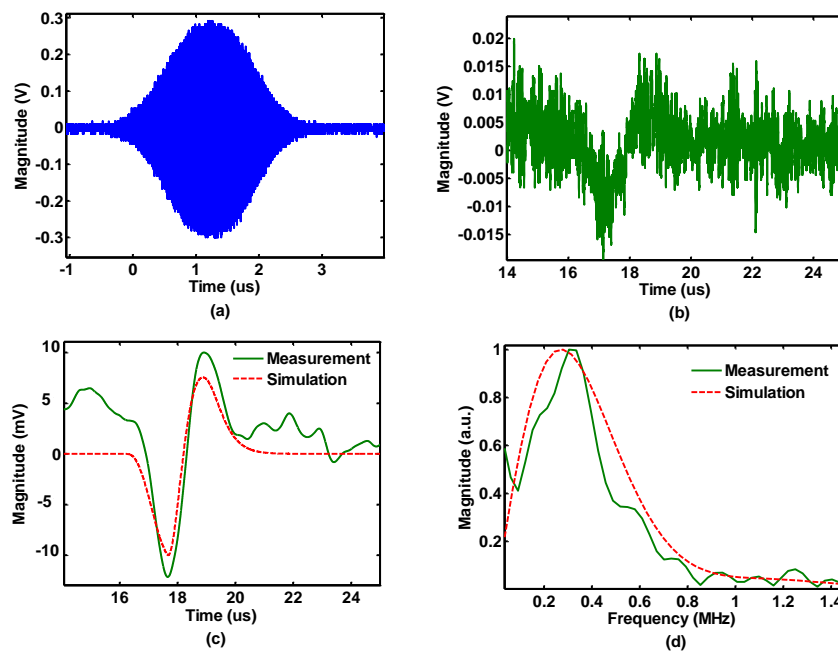

Fig. 12. (a) Experiment measured scattering microwave signal and (b) thermoacoustic signal. (c)
385   Low-pass filtered thermoacoustic signal of measurement and circuit simulation in time domain. (d) Thermoacoustic signal spectrum of measurement and circuit simulation.

Four kinds of porcine tissues (kidney, liver, muscle, fat) with different dielectric constants are prepared. Made in small round shape with 5mm diameter, the tissue is placed close to both the antenna and the transducer. The recorded raw microwave and thermoacoustic wave
390   of muscle tissue are shown in Fig. 12(a)-(b) without data averaging for fair comparison with circuit simulation. After low-pass filtering, the thermoacoustic wave in time and frequency domain is shown in Fig. 12(c)-(d) with green solid lines. To compare the measured results with circuit simulation results based on the equivalent circuit model, we substitute the biological parameters (permittivity and conductivity) of these four tissues in table IV into the

model to obtain the concerned circuit parameters listed in table V. Stimulated by 440 MHz Gaussian modulated source with 2 µs pulse width, the circuit simulated thermoacoustic signal is shown in time and frequency domain in Fig. 12(c)-(d) in red dotted lines. Compared with measured waveform in Fig. 12(c)-(d) in green solid lines, they display comparable time and frequency domain characteristics.

TABLE IV
DIELECTRIC CONSTANT OF FOUR BIOLOGICAL TISSUES AT 440 MHz

Tissue	Fat	Liver	Muscle	Kidney
ε_r	5.5641	50.583	56.823	65.263
σ (S/m)	0.0417	0.6704	0.8066	1.1209

400

TABLE V
CONCERNED CIRCUIT PARAMETERS OF FOUR BIOLOGICAL TISSUES

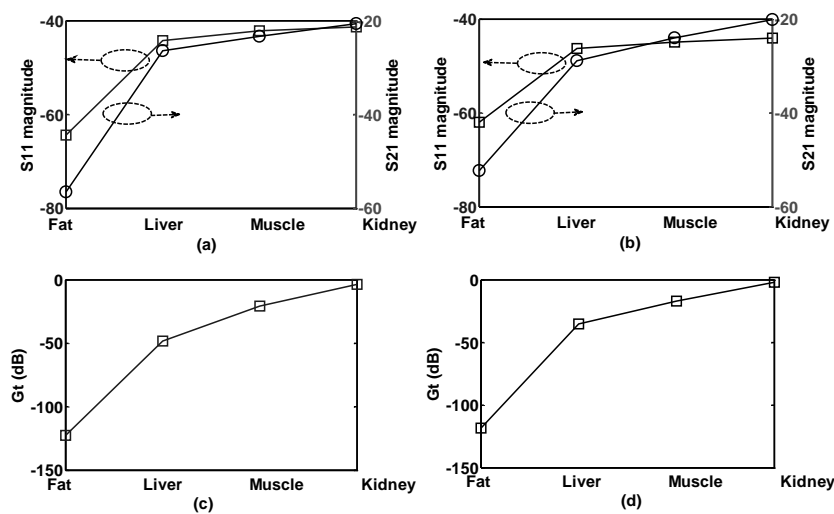| Tissue	Fat	Liver	Muscle	Kidney
$Z_{TL-tissue}$ (Ohm)	$4.7204\times10^{-4}+$ $j3.1667\times10^{-5}$	$1.5439\times10^{-4}+$ $j1.8145\times10^{-5}$	$1.4524\times10^{-4}+$ $j1.8246\times10^{-5}$	$1.3412\times10^{-4}+$ $j2.0241\times10^{-5}$
$G_{TL-tissue}$ (S)	2109	6388.8	6778.2	7290.1
$C_{TL-tissue}$ (F)	2.2518×10^{-8}	1.1950×10^{-7}	1.3552×10^{-7}	1.7510×10^{-7}
K	1.3659×10^{4}	2.1960×10^{5}	2.6421×10^{5}	3.6717×10^{5}

Fig. 13 Magnitude of S_{11} and S_{21} of experiment measurement (a), circuit simulation (b), and their respective transducer gain in (c)-(d) for four different biological tissues at 440 MHz.

S_{11}, S_{21} and transducer gain G_T are all calculated and shown in Fig. 13. Compatible with simulation results in Fig. 9, they demonstrate same characteristic, i.e., S_{11}, S_{21} and G_T are all increasing with larger dielectric contrast between tissue and mineral oil.

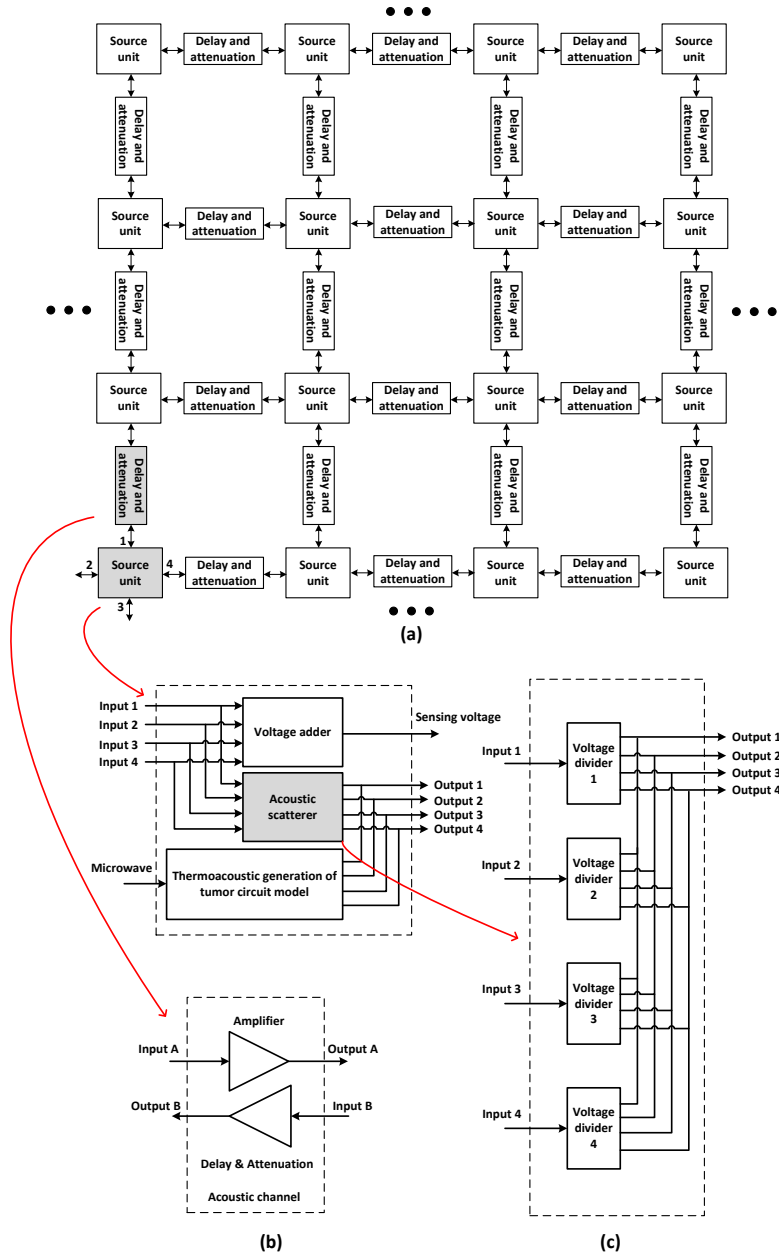## VI. 2D CIRCUIT NETWORK MODELLING FOR HETEROGENEOUS SCENARIOS

Fig. 14. (a) 2D circuit network modeling incorporating the spatial information and heterogeneous situations. (b) Circuit structures of the source unit and acoustic channel blocks. (c) Circuit structure of the acoustic scatterer block.

In the previous sections, a complete circuit model of the tumor is fully described assuming that the tumor is small enough to be treated as an ideal point source, where no spatial information and heterogeneous situations are included. In this section, the circuit model of an ideal point is extended to a 2D circuit network as shown in Fig. 14(a), where two main building blocks are the source unit at every grid, and acoustic channel linking the adjacent source unit, which is with the acoustic delay and attenuation characteristics. By assigning each grid with specific parameters for source unit and acoustic channels, it enables the 2D circuit simulation of heterogeneous medium, which is a significant step closer to the real human body situations. The details of the circuit network modeling will be discussed in details as below.

VI.A. Source unit

To simplify the circuit network modeling, every source unit is only connected with the adjacent four source units in vertical and horizontal directions. Therefore, the four inputs and four outputs in Fig. 14(b) represent the input and output in the top, left, bottom and right directions of the grid, respectively. The building blocks of the source unit include voltage adder, acoustic scatterer, and the thermoacoustic generation of the tumor circuit model.

The voltage adder performs the summation of the four input voltage signals from four directions, which represent the acoustic propagation towards the source unit. Thus the sensing voltage is used to monitor the acoustic pressure at this source unit:

$$p_{\text{unit}} = v_{\text{sensing}} = v_{\text{input 1}} + v_{\text{input 2}} + v_{\text{input 3}} + v_{\text{input 4}}. \quad (44)$$

The voltage scatterer performs the acoustic scattering effect during its propagation through each grid and will be discussed later. The thermoacoustic generation of the tumor circuit model is copied from the previous sections, where the microwave comes in, and acoustic wave goes out. One difference is that the tumor model here has four outputs, representing the wave generation and propagation towards all four the directions, which are added with the outputs of the acoustic scatterer to give the final outputs following the acoustic superposition phenomenon.

VI.B. Acoustic channel

Acoustic channel circuit model is used to model the acoustic wave propagation between adjacent grids, where the delay and attenuations are two key parameters to characterize the acoustic channel. Here two ideal amplifiers with tunable delay and attenuation parameters are

employed to model the bi-directional acoustic propagations. To define the two parameters, we assume that the grid size (distance between two adjacent grids) is d_{grid} (mm), and the acoustic attenuation is α_{grid} (dB/mm). Then the delay and gain parameters of the amplifier in the circuit model are obtained by:

$$
\begin{aligned}
delay &= d_{\text{grid}}/c \ (\mu\text{s}) \\
attenuation &= \alpha_{\text{grid}}d_{\text{grid}} \ (\text{dB}),
\end{aligned}
\tag{45}
$$

where c is the acoustic velocity (~1500 mm/μs in soft tissues). Then the acoustic channel is properly modeled by the circuit blocks with delay and attenuation characteristics.

VI.C. Acoustic scatterer

The acoustic scatterer in the source unit is used to model the acoustic scattering effect of the incident acoustic wave from all four directions. As shown in Fig. 14(c), the acoustic scatterer is comprised of four voltage dividers, where each divider is used to divide the input signal from each direction into four output signals. By doing so, acoustic wave coming in from each direction is scattered into four acoustic waves coming out to adjacent grids. Therefore, there are totally 16 scattering coefficients to be defined as $S_{m,n}, 1 \le m \le 4, 1 \le n \le 4$, where $S_{m,n}$ is the acoustic scattering coefficient from input m to output n, which follows:

$$
\sum_{n=1}^{4} S_{m,n} = 1, 1 \le m \le 4.
\tag{46}
$$

Among all the 16 coefficients, four of them are representing the direct reflection of acoustic wave: $S_{1,1}$, $S_{2,2}$, $S_{3,3}$ and $S_{4,4}$, which are related with the acoustic reflection coefficient in Eq. (35) expressed as:

$$
S_{m,m} = \left| \frac{\dfrac{R_{\text{grid}}}{R_{\text{grid}\pm1}} - 1}{\dfrac{R_{\text{grid}}}{R_{\text{grid}\pm1}} + 1} \right| = \left| \frac{\dfrac{\rho_{\text{grid}}c_{\text{grid}}}{\rho_{\text{grid}\pm1}c_{\text{grid}\pm1}} - 1}{\dfrac{\rho_{\text{grid}}c_{\text{grid}}}{\rho_{\text{grid}\pm1}c_{\text{grid}\pm1}} + 1} \right|, 1 \le m \le 4,
\tag{47}
$$

where R_{grid} and $R_{\text{grid}\pm1}$ are the acoustic impedances of the scatterer's grid and its adjacent grid, ρ_{grid}, $\rho_{\text{grid}\pm1}$, c_{grid} and $c_{\text{grid}\pm1}$ are the respective densities and acoustic velocities. In homogeneous medium, $S_{m,m} = 0$ at each grid, while in heterogeneous medium $S_{m,m} \ne 0$ determined by the acoustic impedance mismatch.

25

465   In addition, another eight acoustic scattering coefficients ($S_{1,2}, S_{1,4}, S_{2,1}, S_{2,3}, S_{3,2}, S_{3,4}, S_{4,1},$ $S_{4,3}$) represent the acoustic scattering effect from one input port to its adjacent two output ports. Similarly, the remaining four acoustic scattering coefficients ($S_{1,3}, S_{2,4}, S_{3,1}, S_{4,2}$) are modeling the direct transmission of acoustic wave through the grid.
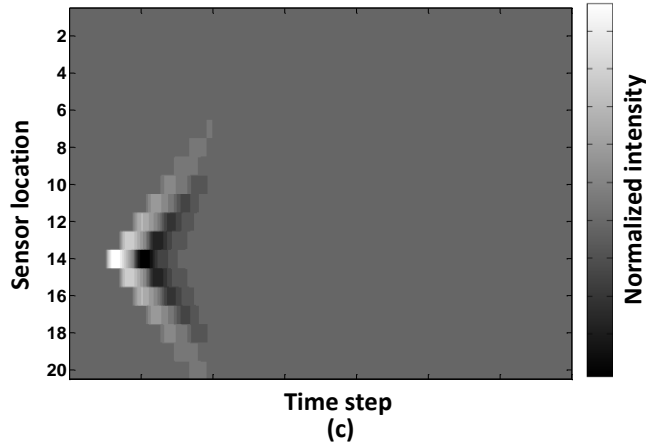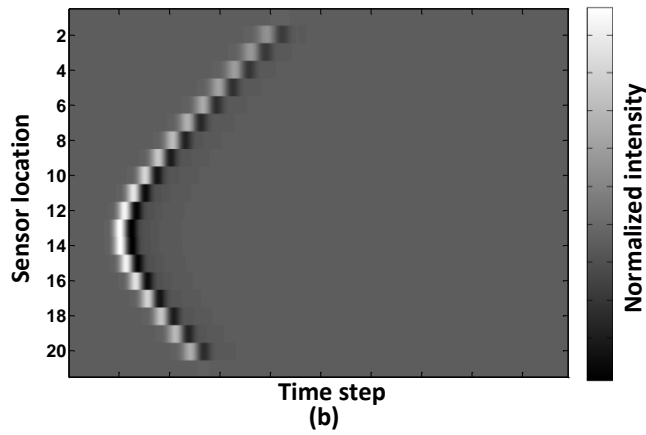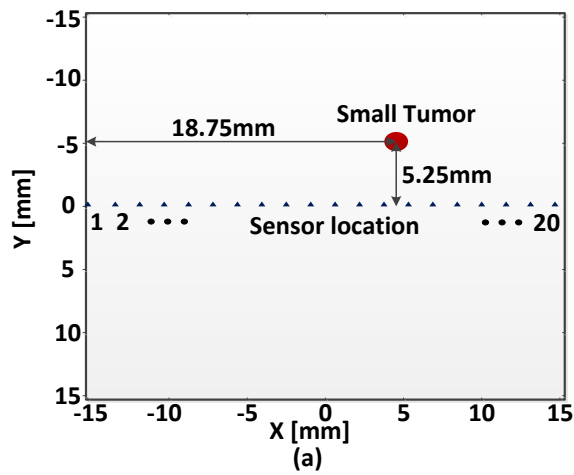

470   **VII. 2D SIMULATION COMPARISON**

26

Fig. 15. (a) 2D simulation model of a single small tumor for both numerical and circuit simulation approaches. (b) The acoustic signals detected by 20 linear array acoustic sensors using numerical simulation, and (c) circuit simulations.

475 To validate the 2D circuit network modeling of microwave acoustic interaction with biological tissues, circuit simulation and numerical simulation are conducted and compared in this section for three different scenarios. The simulation model is shown in Fig. 15(a), where the 30mm×30mm region is segmented by numerous small grids with $d_{grid} = 0.15\,mm$ grid size. Gaussian modulated microwave source with 1 GHz central frequency and 0.1 μs pulse-

480 width is assigned to every unit source in the circuit model, assuming the homogeneous microwave illumination on the region of interest. A total amount of 20 acoustic sensors are aligned at $y = 0$ with 1.5 mm spacing. The propagation delay between adjacent grids is obtained by $delay = d_{grid} / c = 0.1\,\mu s$, and the attenuation is calculated by $\alpha_{grid} d_{grid} = 0.01125\,dB$ in fat tissues.

485 **VII.A. One tumor case**

In the first simulation case, one small tumor with 1.5 mm diameter is embedded at location (18.75 mm, 5.25 mm) in the homogeneous fat tissues, as shown in Fig. 15(a). The physical and circuit parameters of the tumor remain same with the previous simulation in section IV. The acoustic signals detected by the 20 sensors are shown in Fig. 15(b)-(c), simulated by the

490 numerical and circuit approaches. It shows a good agreement in terms of delay and attenuation information: when the sensor is nearer to the tumor source, the acoustic signal has shorter delay and stronger strength due to less attenuation.

VII.B. Two tumor case

In the second simulation case, two tumors with different sizes and locations are included.

495 A smaller tumor is located at (8.25 mm, 2.25 mm) with 1.5 mm diameter, and a larger tumor is located at (18.75 mm, 6 mm) with 3 mm diameter, as shown in Fig. 16(a). The acoustic signals detected by the 20 sensors are shown in Fig. 16(b)-(c), simulated by the numerical and circuit approaches. As expected, smaller tumor gives a narrower acoustic pulse width and reaches the sensor #6 in the earliest time with strongest magnitude; larger tumor gives a

500 broader acoustic pulse width and reaches the sensor #14 first with longer delay time and weaker signal strength.
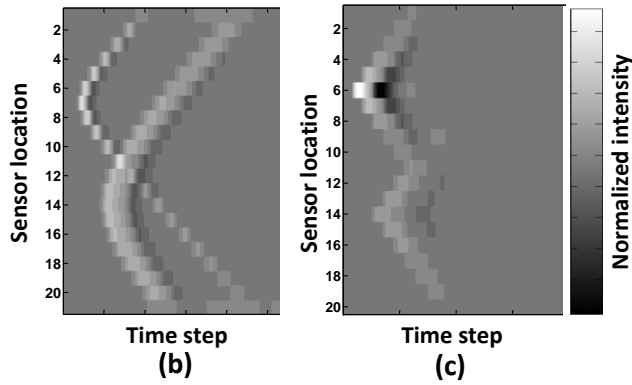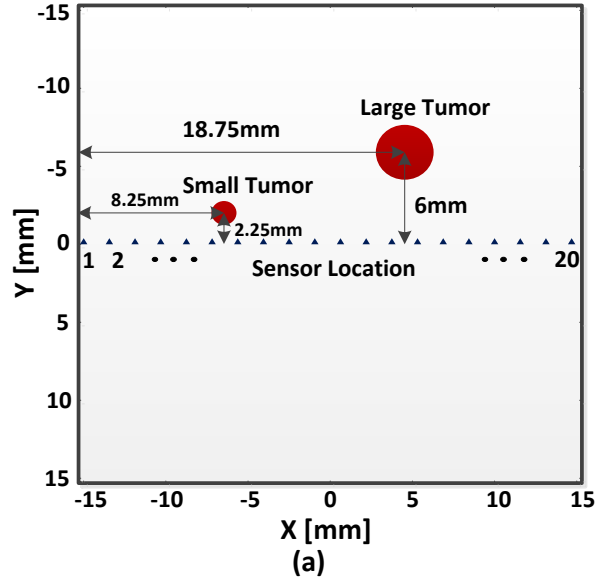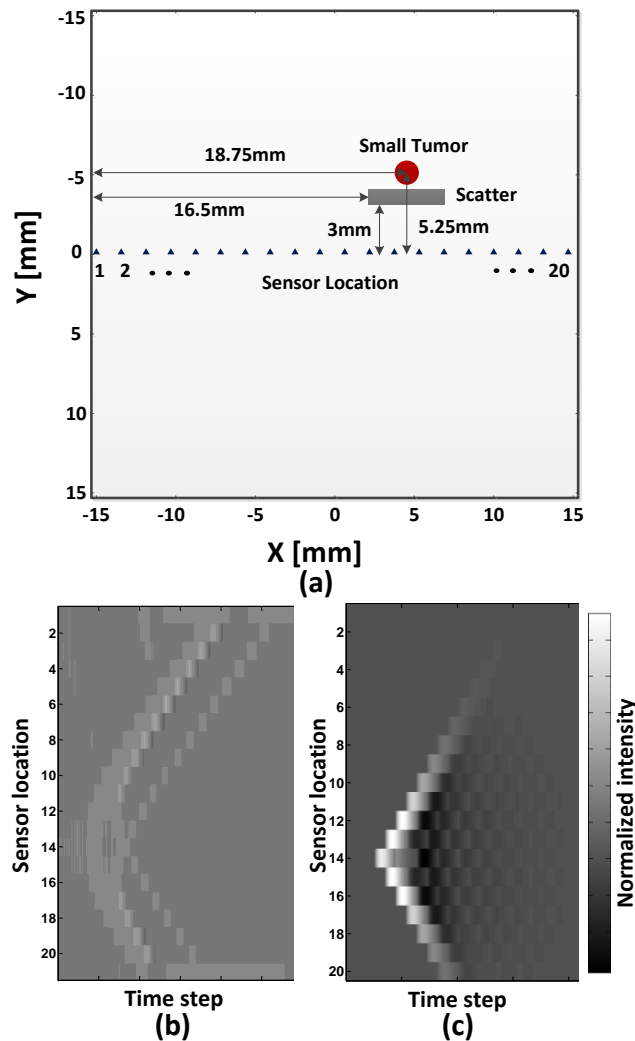
Fig. 16. (a) 2D simulation model of two tumors with different sizes for both numerical and circuit simulation approaches. (b) The acoustic signals detected by 20 linear array acoustic sensors using numerical simulation, and (c) circuit simulations.

VII.C. Acoustic scattering case

In the third simulation case, one tumor and one heterogeneous acoustic scatterer are embedded in the model to mimic the strong acoustic distortion during its propagation, which is shown in Fig. 17(a). The small tumor is located at (18.75 mm, 5.25 mm) with 1.5 mm diameter, and the scatterer has a rectangular shape with 4.5 mm length and 1 mm width, which is located 2 mm below the small tumor. The acoustic velocity and density of the scatterer are set to be 4 mm/μs and 1500 kg/m^3, which are close to the bone in the human body. The acoustic signals detected by the 20 sensors are shown in Fig. 17(b)-(c), simulated by the numerical and circuit approaches. Due to the existence of the strong acoustic scatterer, the acoustic signals detected by the sensors near the scatterer (#12~#16) are severely distorted in both numerical and circuit simulations. In this case, the circuit simulation performs very well when acoustic scatters exist, validating the proposed 2D circuit network

to model the heterogeneous medium, which is a significant step closer to the real biological tissues, e.g. human breast.

520

Fig. 17. (a) 2D simulation model of one tumor and one acoustic scatterer for both numerical and circuit simulation approaches. (b) The acoustic signals detected by 20 linear array acoustic sensors using numerical simulation, and (c) circuit simulations.

VIII. DISCUSSION AND CONCLUSION

525

As the pioneer attempt to build an electrical circuit model to simulate the microwave acoustic bio-effect, the study of this paper provides an alternative simulation approach beyond conventional numerical methods. More importantly, the circuit modeling of the bio-effect enables, for the first time, the co-design and co-simulation of both the microwave acoustic bio-effect and the hardware circuit and system in a uniform circuit simulation environment such as SPICE. The setup of co-design and simulation is shown in Fig. 18,

530

29

where the microwave acoustic bio-effect simulation and hardware simulation are seamlessly combined. By adjusting and optimizing the parameters of the microwave acoustic interaction block and microwave acoustic transceiver block simultaneously, the microwave acoustic imaging system will be developed with optimized performance for possible early-stage cancer detection. An example for the global optimization shown in Fig. 18 combining bio-effect simulation and hardware simulation is to study how parameter A (e.g. conductivity of cancerous tissue) in the bio-effect simulation is related with the parameter B (e.g. input-referred noise of preamplifier) in imaging circuit design. It is unavailable in existing simulation tools and suffering low efficiency in conventional separate simulations. However, it becomes feasible if integrating both simulations in one circuit simulator, then the curve showing the relationship between cancerous tissue's conductivity and preamplifier's noise could be readily simulated to optimize the noise performance subjected to biological tissue's dielectric properties. Furthermore, other microwave-acoustic bio-effect parameters (permittivity, tumor size/density, acoustic velocity, attenuation, etc.) and hardware parameters (microwave power/frequency, gain of amplifier, bandwidth of filter, resolution and sampling rate of analog-to-digital converter (ADC), etc.) could be co-designed and optimized globally in a uniform simulator.
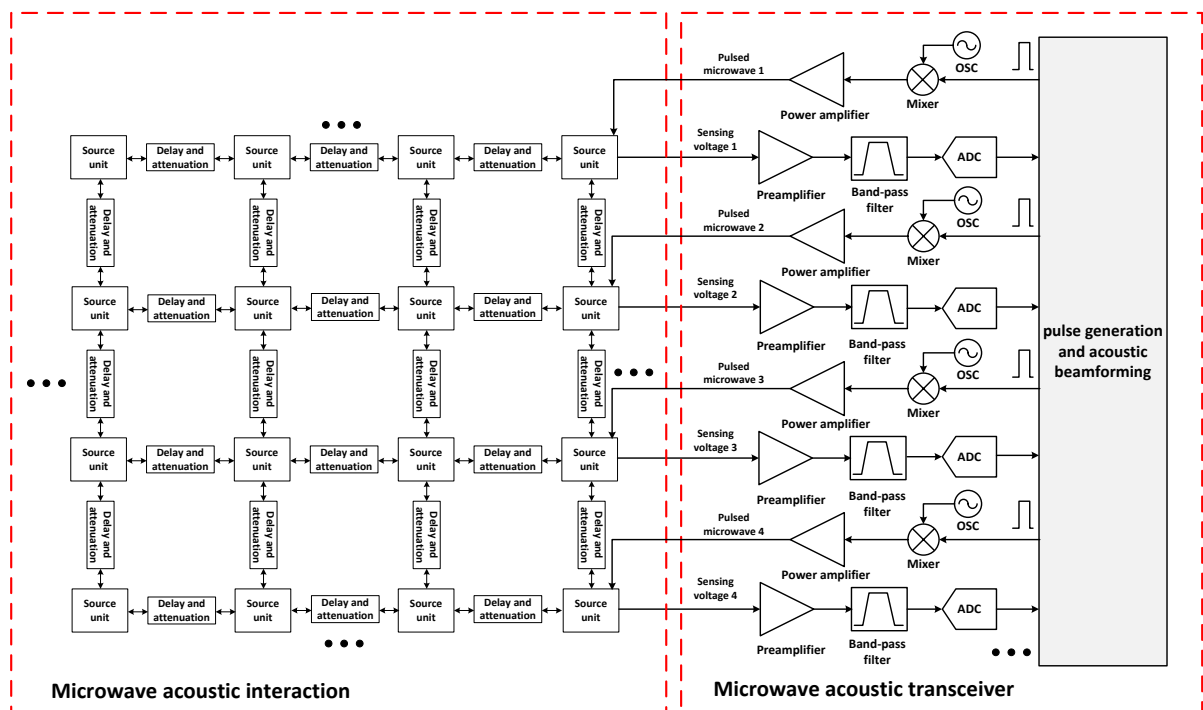

Fig. 18. Co-design and simulation of microwave acoustic bio-effect and transceiver circuit for microwave acoustic imaging system development in a uniform circuit simulator. Pulsed microwave is generated by mixing the pulse signal with microwave source from the oscillator, and fed into the

microwave input port of the unit source. Sensing voltage from the unit source is acquired by the preamplifier, bank-pass filter and ADC to perform the image reconstruction in digital domain.

555   In this paper we have proposed an equivalent circuit model to simulate the microwave acoustic interaction with biological tissues, a faster system-level simulation using SPICE is enabled. Then based on the circuit model, a characteristic gain to quantitatively evaluate the performance of microwave acoustic imaging system is proposed, utilizing the transducer gain derived from the equivalent circuit modeling. This characteristic gain is also a more sensitive
560   indicator than microwave scattering related S_{11} and microwave absorption related S_{21} alone in characterizing the tumor tissues even when in their early stage. From the expression (42), it is easy to derive the design guideline for the optimization of a microwave acoustic imaging system for cancer detection. Numerical simulation and experimental measurement are conducted to verify the validity of the equivalent circuit model. To extend the proposed
565   circuit simulation approach for a more realistic situation to consider acoustic heterogeneity, a 2D circuit network is further proposed comprising source unit and acoustic channel blocks. Simulation results of numerical and circuit approaches agree well for tumors with different sizes and strong acoustic scattering cases. In summary, with the proposed 2D circuit network model, co-simulation fusing microwave acoustic bio-effect and hardware development is
570   becoming possible in a uniform circuit simulator. Hence global optimization becomes feasible for the integrated circuit (IC) implementation of the microwave acoustic imaging system for earlier-stage cancer detection.

ACKNOWLEDGEMENT

REFERENCE:

580   1. S. P. Poplack, T. D. Tosteson, W. A. Wells, B. W. Pogue, P. M. Meaney, A. Hartov, C. A. Kogel, S. K. Soho, J. J. Gibson, and K. D. Paulsen, "Electromagnetic breast imaging: Results of a pilot study in women with abnormal mammograms," Radiology **243,** 350 (2007).

2. C. Gabriel, S. Gabriel and E. Corthout, "The dielectric properties of biological tissues .I. Literature survey," Phys Med Biol **41**, 2231-2249 (1996).

585   3. M. Lazebnik, D. Popovic, L. McCartney, C. B. Watkins, M. J. Lindstrom, J. Harter, S. Sewall, T. Ogilvie, A. Magliocco, T. M. Breslin, W. Temple, D. Mew, J. H. Booske, M. Okoniewski and S. C. Hagness, "A large-scale study of the ultrawideband microwave dielectric properties of normal, benign and malignant breast tissues obtained from cancer surgeries," Phys Med Biol **52**, 6093-6115 (2007).

590   4. W. T. Joines, Y. Zhang, C. X. Li and R. L. Jirtle, "The Measured Electrical-Properties of Normal and Malignant Human Tissues from 50 to 900 Mhz," Med Phys **21**, 547-550 (1994).

5. S. K. Davis, B. D. Van Veen, S. C. Hagness and F. Kelcz, "Breast tumor characterization based on ultrawideband microwave backscatter," IEEE Trans. Biomed. Eng. **55**, 237-246 (2008).

6. E. Kirshin, B. Oreshkin, G. K. Zhu, M. Popovic and M. Coates, "Microwave Radar and Microwave-Induced Thermoacoustics: Dual-Modality Approach for Breast Cancer Detection," IEEE Trans. Biomed. Eng. **60**, 354-360 (2013).

595

7. F. Gao and Y. J. Zheng, "A Correlated Microwave-Acoustic Imaging Method for Early-Stage Cancer Detection," 2012 Annual International Conference of the IEEE Engineering in Medicine and Biology Society (EMBC), 480-483 (2012).

600   8. F. Gao, Y. J. Zheng and D. F. Wang, "Microwave-acoustic phasoscopy for tissue characterization," Appl Phys Lett **101**, 043702 (2012).

9. E. Fear, X. Li, S. Hagness, and M. Stuchly, "Confocal microwave imaging for breast cancer detection: Localization of tumors in three dimensions," IEEE Trans. Biomed. Eng., **49**, 812-822 (2002).

605   10. P. M. Meaney, M. W. Fanning, D. Li, S. P. Poplack and K. D. Paulsen, "A clinical prototype for active microwave imaging of the breast," IEEE Trans. Microw. Theory Tech. **48**, 1841-1853 (2000).

11. P. M. Meaney, E. Demidenko, N. K. Yagnamurthy, D. Li, M. W. Fanning and K. D. Paulsen, "A two-stage microwave image reconstruction procedure for improved internal feature extraction," 610   Med Phys **28**, 2358-2369 (2001).

12. Y. Xie, B. Guo, L. Xu, J. Li, and P. Stoica, "Multistatic adaptive microwave imaging for early breast cancer detection," IEEE Trans. Biomed. Eng., **53**, 1647-1657 (2006).

13. J. Sill and E. Fear, "Tissue sensing adaptive radar for breast cancer detection—Experimental investigation of simple tumor models," IEEE Trans. Microw. Theory Tech. **53**, 3312-3319 (2005).

14. H. B. Jiang, C. Q. Li, D. Pearlstone and L. L. Fajardo, "Ultrasound-guided microwave imaging of breast cancer: Tissue phantom and pilot clinical experiments," Med Phys **32**, 2528-2535 (2005).

15. X. H. Feng, F. Gao and Y. J. Zheng, "Magnetically mediated thermoacoustic imaging toward deeper penetration," Appl. Phys. Lett. **103,** 083704 (2013).

16. D. Q. Piao, R. A. Towner, N. Smith and W. R. Chen, "Magnetothermoacoustics from magnetic nanoparticles by short bursting or frequency chirped alternating magnetic field: A theoretical feasibility analysis," Med Phys **40,** 063301 (2013).

17. Z. Ji, C. G. Lou, S. H. Yang and D. Xing, "Three-dimensional thermoacoustic imaging for early breast cancer detection," Med Phys **39**, 6738-6744 (2012).

18. D. Razansky, S. Kellnberger and V. Ntziachristos, "Near-field radiofrequency thermoacoustic tomography with impulse excitation," Med Phys **37**, 4602-4607 (2010).

19. M. Omar, S. Kellnberger, G. Sergiadis, D. Razansky and V. Ntziachristos, "Near-field thermoacoustic imaging with transmission line pulsers," Med Phys **39**, 4460-4466 (2012).

20. L. Yao, G. F. Guo and H. B. Jiang, "Quantitative microwave-induced thermoacoustic tomography," Med Phys **37**, 3752-3759 (2010).

21. F. Gao, Y. J. Zheng, X. H. Feng and Claus-Dieter Ohl, "Thermoacoustic resonance effect and circuit modelling of biological tissue," Appl. Phys. Lett. **102**, 063702 (2013).

22. A. Taflove and S. C. Hagness, *Computational Electrodynamics: The Finite-Difference Time-Domain Method*, 3rd ed. Boston, MA: Artech House, Jul. 2005.

23. B. Guo , J. Li , H. Zmuda and M. Sheplak, "Multi-frequency microwave induced thermal acoustic imaging for breast cancer detection", IEEE Trans. Biomed. Eng., **54**, 2000-2010 (2007).

24. Y. Xie, B. Guo, J. Li, G. Ku, and L. V. Wang, "Adaptive and robust methods of reconstruction for thermoacoustic tomography, " IEEE Trans. Biomed. Eng., **55**, 2741-2752 (2008).

25. Frank S. Barnes, Ben Greenebaum, *Bioengineering and Biophysical Aspects of Electromagnetic Fields*, Boca Raton : CRC/Taylor & Francis, 2007.

26. C. H. Li and L. H. V. Wang, "Photoacoustic tomography and sensing in biomedicine," Phys Med Biol **54**, R59-R97 (2009).

27. A. R. Fisher, A. J. Schissler and J. C. Schotland, "Photoacoustic effect for multiply scattered light," Phys Rev E **76** (2007).

28. C. G. Lou and D. Xing, "Photoacoustic measurement of liquid viscosity," Appl Phys Lett **96** (2010).

29. Anant Agarwal and Jeffrey H. Lang, *Foundations of Analog and Digital Electronic Circuits*, Boston : Elsevier : Morgan Kaufman Publishers, 2005, chapter 12.6, pp 678a-678j.

30. Kinsler L. E., Frey A. R., Coppens A. B. and Sanders J. V., *Fundamentals of Acoustics*, John Wiley and Sons, 2000, p. 213.

650 31. Sophocles J. Orfanidis, "Electromagnetic Waves and Antennas", [Online] , Available: http://eceweb1.rutgers.edu/~orfanidi/ewa/

32. F. A. Duck*, Physical Properties of Tissue*. London, U.K.: Academic, 1990.

33. D. R. Reinecke, R. A. Kruger, R. B. Lam and S. P. Del Rio, "Co-registered photoacoustic, thermoacoustic and ultrasound mouse imaging," Proc. SPIE Photons Plus Ultrasound: Imaging

655 and Sensing 2010 **756420** (2010).

34. J. J. Niederhauser , M. Jaeger , R. Lemor , P. Weber and M. Frenz "Combined ultrasound and optoacoustic system for real-time high contrast vascular imaging", IEEE Trans. Med. Imag., **24**, 436-440 (2005).

35. A. B. Karpiouk, S. R. Aglyamov, S. Mallidi, J. Shah, W. G. Scott, J. M. Rubin and S. Y.
660 Emelianov, "Combined ultrasound and photoacoustic imaging to detect and stage deep vein thrombosis: phantom and ex vivo studies," J Biomed Opt **13**, 054061 (2008).

36. R. K. Amineh, M. Ravan, A. Trehan, and N. K. Nikolova, "Near-field microwave imaging based on aperture raster scanning with TEM horn antennas," IEEE Trans. Antennas Propag., **59**, 928-940 (2011).

665 37. K. Maslov and L. V. Wang, "Photoacoustic imaging of biological tissue with intensity-modulated continuous-wave laser," J Biomed Opt **13**, 024006 (2008).